

www.acsnano.org

Insight into the Spin Properties in Undoped and Mn-Doped CdSe/CdS-Seeded Nanorods by Optically Detected Magnetic Resonance

Joanna Dehnel, Yahel Barak, Itay Meir, Adam K. Budniak, Anjani P. Nagvenkar, Daniel R. Gamelin, and Efrat Lifshitz*



Cite This: ACS Nano 2020, 14, 13478–13490



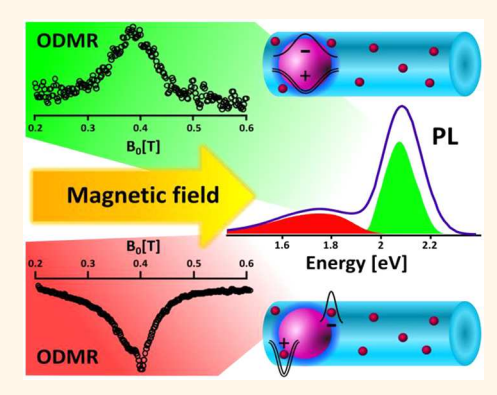
ACCESS

Metrics & More

Article Recommendations

s Supporting Information

ABSTRACT: Controlling the spin degrees of freedom of photogenerated species in semiconductor nanostructures via magnetic doping is an emerging scientific field that may play an important role in the development of new spin-based technologies. The current work explores spin properties in colloidal CdSe/CdS:Mn seeded-nanorod structures doped with a dilute concentration of Mn²⁺ ions across the rods. The spin properties were determined using continuous-wave optically detected magnetic resonance (ODMR) spectroscopy recorded under variable microwave chopping frequencies. These experiments enabled the deconvolution of a few different radiative recombination processes: band-to-band, trap-to-band, and trap-to-trap emission. The results uncovered the major role of carrier trapping on the spin properties of elongated structures. The magnetic parameters, determined through spin-Hamiltonian simulation of the steady-state ODMR spectra, reflect anisotropy associated with carrier trapping at the seed/rod interface. These observations unveiled changes in the carriers' g-



factors and spin-exchange coupling constants as well as extension of radiative and spin-lattice relaxation times due to magnetic coupling between interface carriers and neighboring Mn²⁺ ions. Overall, this work highlights that the spin degrees of freedom in seeded nanorods are governed by interfacial trapping and can be further manipulated by magnetic doping. These results provide insights into anisotropic nanostructure spin properties relevant to future spin-based technologies.

KEYWORDS: seeded nanorods, core/shell interface, magnetic doping, spin properties, optically detected magnetic resonance

odifing the magnetic and magneto-optical properties of nanostructures by incorporating magnetic impurities in bulk, epitaxial, or strain-grown semiconductors has been extensively explored. 1-6 Diluted magnetic semiconductors (DMS), incorporating magnetic impurities at substitutional positions in nominally diamagnetic hosts, 1,8 have also gained high significance in the arena of colloidal semiconductor nanostructures over the last two decades. Colloidal DMS nanostructures such as quantum dots, 9-14 ribbons, 15,16 and nanoplatelets 17,18 of II-VI, III-V, IV-VI, and I-III-V semiconductors have been explored. The exceptionally strong size confinement in colloidal nanostructures engenders strong spin-exchange coupling between magnetic dopants and the injected or photogenerated carriers of the host. Numerous studies have examined doping with transition-metal cations (e.g., Mn²⁺) whose unpaired d-orbital spins interact with s- and p-type carriers, leading to the wellknown sp-d spin-exchange interactions, $^{6,19-22}$ which cause mutual spin alignment of host and dopant spins. Phenomena involving sp-d exchange interaction include optical detection of magnetization fluctuations, ^{23–25} photoinduced exciton-magnetic polaron formation, ^{10,24,26,27} giant band-edge Zeeman splittings, and elongation of carrier spin-coherence times. ^{5,11,28–32} Moreover, formation of core/shell heterostructures enables tunability of the above-mentioned phenomena as a function of mutual spacing between host and dopant spins. ^{17,33–37} Overall, the ability to tailor carrier spin properties in size-confined systems governs their potential utility in quantum computation, ^{38,39} spintronics, ^{40,41} and spin-light emitting diodes. ⁴²

The present study discusses the incorporation of Mn²⁺ ions into asymmetric core/shell QD/nanorod heterostructures,

Received: July 1, 2020
Accepted: September 16, 2020
Published: September 16, 2020





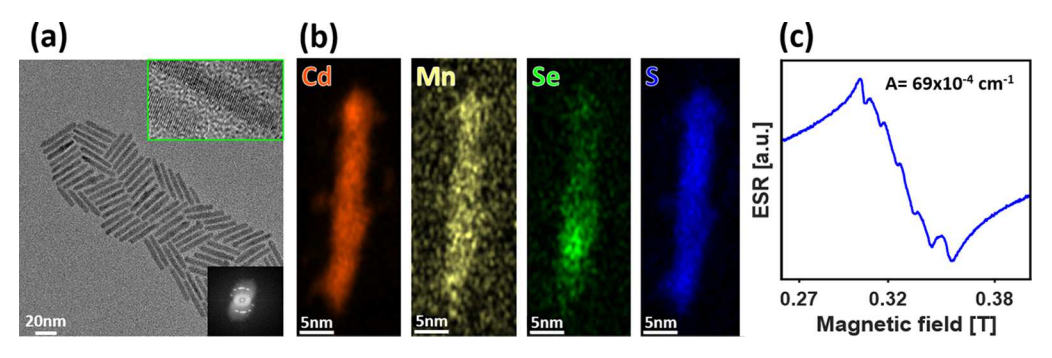


Figure 1. Structural, morphological and compositional properties: (a) A TEM image of an assembly of CdSe/CdS:Mn sNRs. Insets: A HR-TEM image of a single sNR (top) and a corresponding Fourier transform pattern (bottom); (b) STEM-EDX maps of the representative elements in a single CdSe/CdS:Mn sNR; (c) room-temperature ESR spectrum of an assembly of CdSe/CdS:Mn sNRs, recorded with 9.4 GHz microwave radiation.

referred to here as seeded-nanorods (sNRs). The undoped structures exhibit efficient luminescence, with a reduced Auger rates 43,44 relative to those in the parent seed colloidal quantum dots. 45,46 The electronic properties of sNRs are tuned through change in composition and length-to-width aspect ratio.⁴⁷ However, the character of the sNRs' electronic structure has been a matter of concern for many years, showing either a type-II^{49,50} or type-II^{51–53} configuration across the core—shell interface, which can also be tuned by an external electric field.⁵¹ For CdSe/CdS sNRs, various studies have proposed a degeneracy of the core and shell conduction band edges but a large potential barrier of ~0.7 eV in the valence band.⁵¹ Such a configuration localizes the hole within the CdSe seed but permits delocalization of the electron across the entire structure (namely, a type-II configuration). Other reports using scanning tunneling spectroscopy ⁴⁹ or quasi-continuous photoluminescence⁴⁸ have shown a positive barrier of 0.3 eV of confining electrons within the seed, emanating from a strong electron-hole Coulomb interaction (resulting in type-I configuration). All the above-mentioned studies signify a dominant regulation of the electronic structure by the seed diameter, wherein a transition from type-II to type-I configuration entails a threshold diameter of 2.8 nm in relatively thin-shell nanostructures.⁴⁸ With the exception of giant-shell nanostructures, the rod dimensions have only a minor influence, presumably stemming from the extremely small exciton Bohr radius (<3 nm) in CdS. Notably, the elongated shape and partial charge separation in the type-II alignment endow CdSe/CdS sNRs with improved conductivity for optoelectronic devices (e.g., photovoltaics or photocatalysis).54

Whereas the optical and electrical properties of sNRs have been meticulously researched in recent years, there remains a dearth of fundamental research exploring the spin degrees of freedom in such nanostructures. Two seminal reports exposed the exciton fine structure of sNRs and discussed spin flip processes within the exciton manifold. Another related work reported the investigation of spin properties in simple rods and in undoped core/tetrapod heterostuctures. Only one report revealed spin and magneto-optical properties of diluted magnetic sNRs. None of the above studies dealt with the influence of the core—shell interface on the spin degrees of freedom in these elongated structures, nor did they disclose the interaction of magnetic dopants with trapped carriers at interface sites.

Herein, we investigate the magneto-optical properties of undoped and Mn²⁺-doped CdSe/CdS sNRs with seed

diameters of 3.1 nm and rod dimensions of 30 nm × 4 nm. A dilute concentration of Mn²⁺ ions is incorporated in the rod region, and these doped sNRs are denoted as CdSe/CdS:Mn sNRs. The magneto-optical properties were determined using continuous-wave optically detected magnetic resonance (ODMR) spectroscopy. These investigations have revealed localization of photogenerated carriers either at the core or around the core-shell interface, and hence a type-I configuration of CdSe and CdS band edges. The results have also uncovered a dominant spin coupling between electron and hole carriers at these interfaces with nearby Mn²⁺ ions. Furthermore, frequency-modulated ODMR measurements have allowed differentiation among overlapping recombination emission events, and supply the radiative and spin-lattice relaxation times associated with each emissive excited state. The long radiative and spin relaxation times observed at interface sites are significant for practical applications. The scientific findings in this work shed light on important aspects of spins in nanoscale heterostructures.

RESULTS AND DISCUSSION

The synthesis procedures of undoped and doped sNRs are described in the Supporting Information, while the structural characterization, composition, and basic optical properties of sNRs are outlined as follows. The crystallographic structure and morphology of the nanocrystals were identified using transmission electron microscopy (TEM). An illustrative TEM image of an assembly of CdSe/CdS:Mn sNRs is displayed in Figure 1a, indicating an average seed-diameter of 3.1 nm, embedded in 30 nm × 4 nm CdS rods that deviate slightly in length from the undoped sNRs (32 nm, see Figure S1(a)), presumably due to kinetic inhibition of the rod growth by the impurities. The top and bottom insets in Figure 1a show a high-resolution TEM (HR-TEM) image of a single sNR and a Fourier transform (FT) pattern of the image, respectively. The FT pattern discloses the existence of a wurtzite structure. Energy dispersive X-ray (EDX) maps obtained via scanning TEM (STEM), using 60 keV electron beam, are displayed in Figure 1b, and complementary observations, upon the use of 200 keV are shown in Figure S2. The maps of Cd and S (in both Figure 1b and S2) show homogeneous distributions across the rod, while the Se map shows a bright spot close to one of the ends, revealing the position of the CdSe seed. The Mn map (visible only under 60 keV operation) shows sparsely spread atoms, supporting a relatively low doping concentration. A Mn concentration of 1.2% was determined by

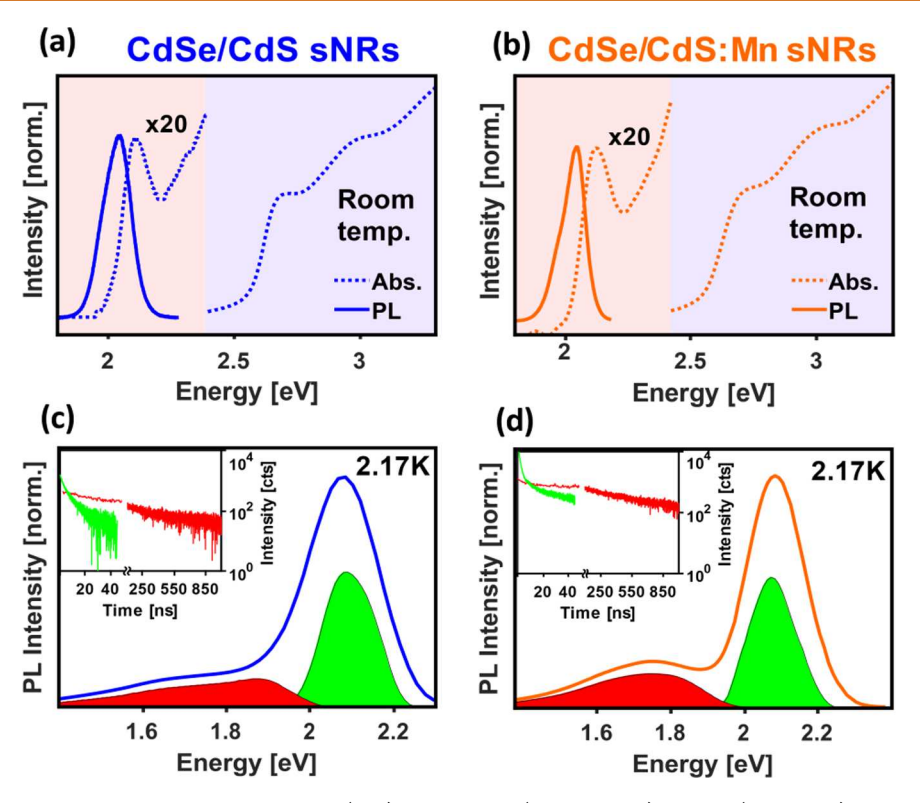


Figure 2. Optical properties of undoped and doped sNRs: (a, b) Absorbance (dashed lines) and PL (bold lines) spectra of CdSe/CdS (a) and CdSe/CdS:Mn sNRs (b), recorded at room temperature. The shaded areas differentiate between optical transitions in the CdSe (low energy) and in CdS (high energy) constituents. (c, d) PL spectra of sNRs as in (a, b), respectively, recorded at 2.17 K. The overlapping green and red bands correspond to the spectra recorded through different optical filters. Insets: PL decay curves of the green and red emission bands.

inductively coupled plasma atomic emission spectroscopy (ICP-AES) analysis.

The Mn²⁺ dopants were examined using ground-state electron spin resonance (ESR) spectroscopy. A representative X band (9.4 GHz) ESR spectrum of CdSe/CdS:Mn sNRs recorded at room temperature is shown in Figure 1c. The broad spectrum is split into six hyperfine signals. This pronounced sextet is primarily related to a resonance transition between electron spin states of a Mn²⁺ ion, $m_s(1/2) \leftrightarrow m_s(-1/2)$ 2), which is split by the hyperfine interaction with nuclear spins (when I = 5/2). The g factor extracted from the ESR spectrum (g = 2.001) is in accordance with that of a covalently bonded Mn²⁺ ion in a II-VI compound at a substitutional position. 64 The hyperfine splitting constant (A) equals (69 \pm $(2) \times 10^{-4}$ cm⁻¹, compatible with the value found in bulk wurtzite CdS:Mn^{65,66} but deviating from that of wurtzite CdSe:Mn $(62 \times 10^{-4} \text{ cm}^{-1})^{67}$ and of a surface site $(85 \times 10^{-4} \text{ cm}^{-1})^{67}$ cm⁻¹).⁶⁸ The broad background line in the ESR spectrum may be due to unresolved Mn-atomistic transitions (e.g., \pm 5/2 \leftrightarrow ± 3/2) in randomly oriented rods and/or to Mn-Mn spindipole coupling.

The absorption and photoluminescence (PL) spectra of CdSe/CdS sNRs recorded at room temperature are shown in Figure 2a. The absorption spectrum includes two separate band-edge regions as highlighted by the shaded backgrounds, referring to the CdSe and CdS constituents from low to high energies, respectively.⁴⁷ The scale of CdSe spectral regime is expanded 20 times relative to that of the CdS edge. The PL spectrum is comprised of a single asymmetric band just below the CdSe absorption onset, generated by photoexcitation above the CdS band-edge energy ($E_{\rm ex} = 3.06$ eV) with a low excitation power (0.24 J/cm²).

The room temperature absorption and PL spectra of CdSe/CdS:Mn sNRs are plotted in Figure 2b and show only minor differences from those of the undoped sNRs. A PL spectrum excited nearly in resonance with the CdSe band edge is shown in Figure S1(b), revealing a similar response to that recorded under nonresonant excitation, hence suggesting the absence of direct recombination from the CdS constituent.

PL spectra of undoped and doped sNRs monitored at a cryogenic temperature (2.17 K) are shown in parts c and d, respectively, of Figure 2, where both spectra show a relatively sharp band around 2.1 eV and an additional weak and wide band at lower energies. The PL components (the colored area under the curve) in (c) and (d) were isolated by recording the spectra with a tunable band-pass (green) or with a low-pass filter (red). The mentioned color notations are used hereafter for classifying the spectral regimes. The PL decay curves of the undoped and doped sNRs recorded at 2.17 K, for green and red bands, are displayed as insets of Figure 2c,d. Those decays were fitted to a biexponential function (see Figure S3) with fast and slow components. The origins of the fast component, although only a minor contribution, are discussed in the SI. A fit to the dominant components in the green spectral regime revealed a lifetime of 15.6 ns in undoped sNRs and 38.1 ns in doped sNRs, viz., illustrating free or bound excitonic characteristics, whereas the red spectral region fit exhibits dominant components with lifetimes of 514 and 634 ns in the undoped and doped sNRs, respectively (see best fit in Figure S3). Such long decay times, along with a huge Stokes shift of ~330 meV below the exciton extrema, allows association of the red bands with trap-recombination processes. Further extension of a lifetime in the doped sNRs with respect to undoped ones, is associated either with the interaction of photo-

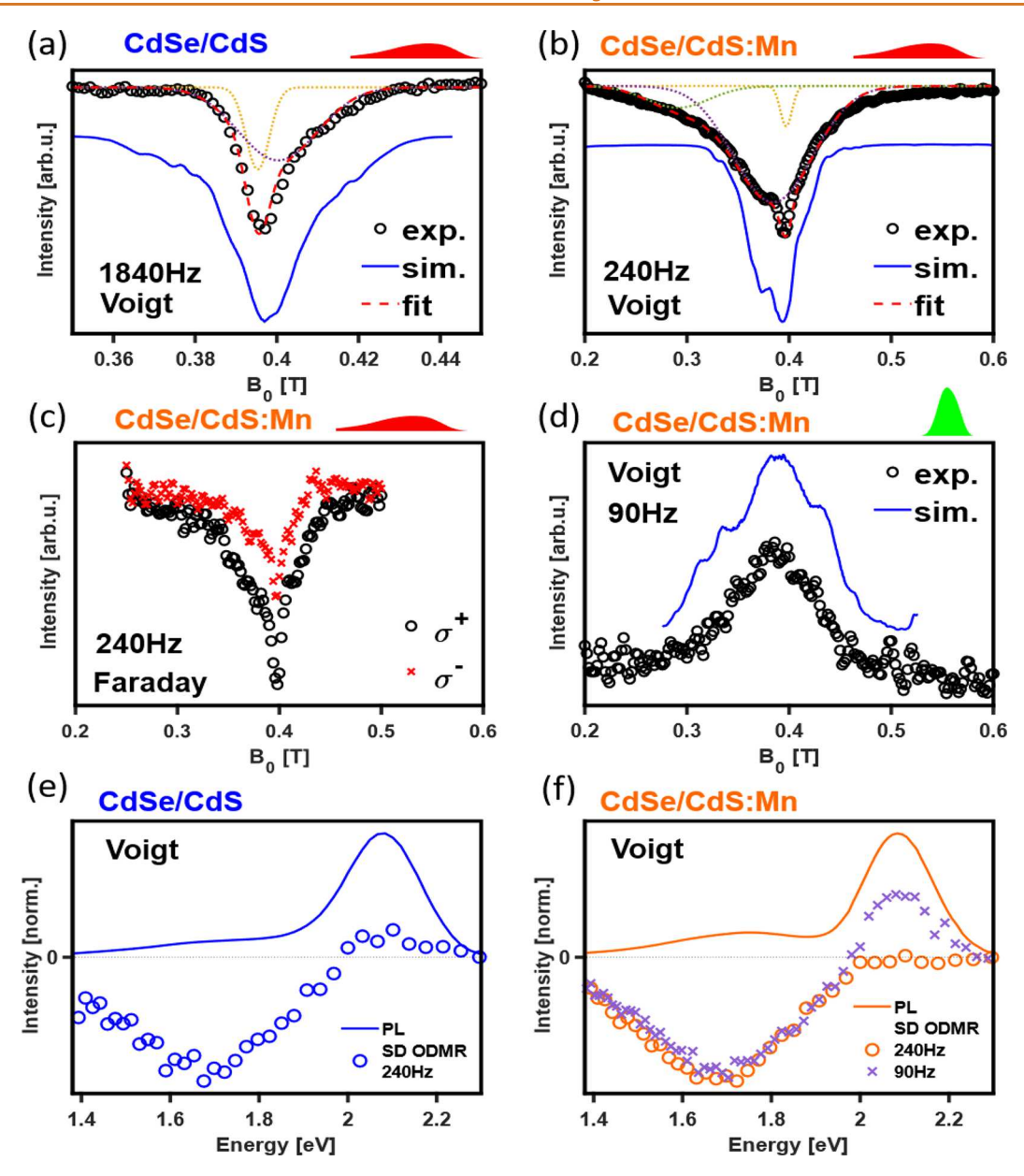


Figure 3. Continuous-wave ODMR observations: (a, b) ODMR spectra of CdSe/CdS (a) and CdSe/CdS:Mn sNRs (b), monitored at the redemission regions under Voigt configuration; (c) ODMR spectra of CdSe/CdS:Mn sNRs, monitored in red-emission region under Faraday configuration; (d) ODMR spectrum of CdSe/CdS:Mn sNRs, monitored at the green-emission region under a Voigt configuration; (e, f) spectral dependence (SD) ODMR spectra of CdSe/CdS (e) and CdSe/CdS:Mn sNRs (f), recorded under magnetic resonance conditions (see text). The used chopping frequencies in each case is labeled on the corresponding panels. The dashed lines are best fit Gaussians to the spectra, while the blue lines in panels (a)–(d) correspond to the simulated spectra.

generated carriers with Mn dopants^{9,69} or linked to self-trapping of carriers produced by a distortion around the dopants. Additionally, the PL spectra of doped and undoped sNRs were further examined under the influence of an external magnetic field (B_0) while monitoring two opposing circularly polarized ($\sigma\pm$) components. A plot of degree of circular polarization (DCP) *versus* strength of the applied magnetic field (from 0 to 8 T) is given in Figure S4. The DCP curve of undoped CdSe/CdS sNRs presents a negative slope, while that of CdSe/CdS:Mn sNRs is initially nonlinear with a plateau of positive values. Such a behavior is a reflection of the sp-d interaction in the presence of a magnetic dopant.

A Mn^{2+} ion has a high-spin alignment of its five *d*-electron spins, with a total spin momentum of $S_{Mn} = 5/2$ (and

projections $m_{\rm S}=\pm 5/2, \pm 3/2, \pm 1/2)$. A hole carrier (at bandedge p-orbital) undergoes a spin-exchange interaction with these Mn²⁺ electrons, while an electron (at band-edge s-orbital) involves a potential (or kinetic s-d)⁷⁰ interaction with Mn²⁺ electrons.³ Moreover, trapped carriers are anticipated to experience an efficient spin interaction with neighboring Mn²⁺ ions due to the conjoint surrounding and long-lived excited state, as often found in bulk semiconductors.^{1,3} The study here accomplished a comprehensive analysis of different spin interactions of band-edge or trapped carriers with the surrounding, through ODMR spectroscopy.

An ODMR spectrum is a plot of a differential change in the emission intensity ($\Delta PL/PL$) *versus* a magnetic resonance parameter (*e.g.*, strength of an external magnetic field).^{71–74} An

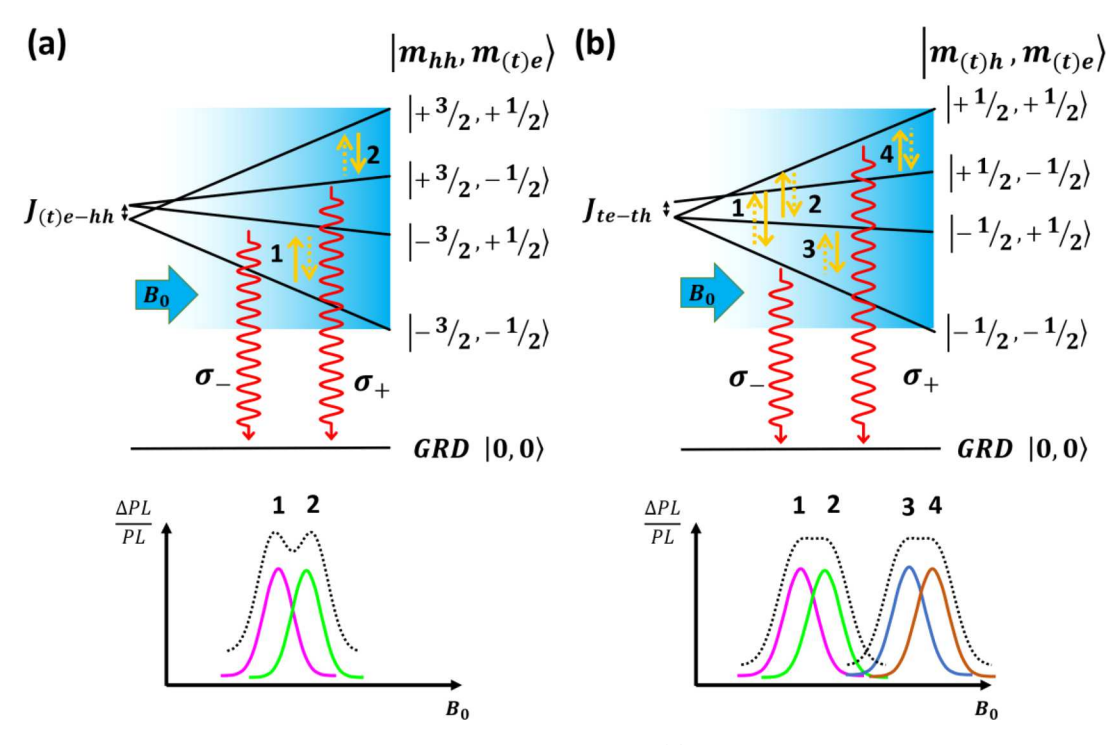


Figure 4. Spin diagram models, demonstrating the magneto-optical transitions: (a) Spin manifold representing the band-to-band or trap-to-band recombination emission, involving valence band hole with angular momentum $J_{hh} = 3/2$ and conduction band or trapped electron with spin momentum $S_{(t)e} = 1/2$. (b) Spin manifold representing the trap-to-trap recombination emission, involving trapped electron and trapped hole each with spin momentum $S_{te,th} = 1/2$. The wavy arrows represent radiative transitions. The yellow arrows indicate magnetic resonance transitions that either quench or enhance the radiative emission intensity. Anticipated ODMR spectra involving luminescence enhancement (an unthermalized process) are shown below the diagrams.

ODMR spectrum resembles a ground-state ESR spectrum, except that the magnetic resonance events take place in the excited state and the resulting change in magnetization is observed through an optical signal. A scheme of the experimental setup is given in the Figure S5. The sample was positioned within a microwave (MW) cavity at the center of an external magnetic field (B₀), and this unit was embedded into a cryostat (operating at 2.17 K). The cavity was coupled to a MW source with a sinusoidal frequency of $v_{\rm MW}$ = 10.76 GHz, where in the B_1 field $(\bot B_0)$ of MW induces magnetic resonance transitions. Simultaneously, the sample was irradiated with a continuous-wave optical beam. The differential emission intensity from the undoped or doped sNRs was monitored selectively at different spectral regimes as per the color scheme in Figure 2c,d and detected under a Voigt $(B_0 \perp k_{\text{excitation}})$ or a Faraday $(B_0 \parallel k_{\text{excitation}})$ alignment (without/ with circularly polarized detection). The MW amplitude was chopped with a square-wave modulator, which acted as a reference signal to the measured emission via a lock-in amplifier. Interestingly, the MW chopping frequency also had a significant influence on the appearance of the ODMR spectrum. This experimental factor was used for deconvoluting overlapped luminescence features as well as for determining radiative/nonradiative and spin-relaxation rates. Furthermore, $\Delta PL/PL$ reflects the mechanism by which a magnetic resonance transition perturbs the radiative transition (quenching versus enhancement).75-77 While an ODMR spectrum involves a plot of $\Delta PL/PL$ versus B_0 in a fixed spectral window, plotting $\Delta PL/PL$ versus a spectral dependence (SD) at a fixed magnetic resonance condition (B_{Max}, v_{MW}) provides complementary information.⁷¹

Figure 3a portrays the ODMR spectrum of undoped CdSe/ CdS sNRs recorded in a Voigt configuration, while monitoring a red band, using a chopping frequency of 1840 Hz. The spectrum has a negative sign when monitored in-phase with respect to the turn-on time of the MW, leading to a $\Delta PL/PL$ of -0.5×10^{-4} to -5.0×10^{-4} . The spectrum itself comprises of two resonances centered around 0.40 and 0.41 T (see fit Gaussians), with average g-Landé factors of 1.941 and 1.903, respectively. Such g-factor values deviate substantially from those of carriers at the valence or conduction band edges, suggesting the involvement of a trapped carrier in the recombination emission. The spectrum in Figure 3b is retained upon increasing the MW power (see Figure S6), thus excluding magnetic coupling to multiple excitons or spin saturation effects. Furthermore, the negative signal as well as its shape stayed intact up to nearly 8000 Hz (vide infra). Under these conditions, negative signals imply a quench of luminescence intensity due to magnetic resonance transitions in the excited state. Figure 3b depicts the ODMR spectrum of the CdSe/CdS:Mn sNRs, recorded in a Voigt configuration by monitoring the red band in Figure 2d with a MW chopping frequency of 240 Hz. The spectrum consists of a few different components (Gaussian fits are shown as thin lines): a sharp negative resonance resembling that in the undoped sample; a broad negative band with a weak fine structure; and a broad and weak resonance at low field. Certainly, the ODMR spectrum of the doped sNRs differs considerably from that of the undoped sNRs, presumably due to the interaction of photogenerated carriers with nearby Mn2+ spins. This assumption will be corroborated below using a spin Hamiltonian simulation of the spectrum. Simulated spectra of both undoped and doped sNRs ODMR resonances are

represented as blue bold lines in Figure 3a,b. Figure 3c shows the ODMR spectrum of CdSe/CdS:Mn sNRs monitored in the red spectral regime using a chopping frequency of 240 Hz with a Faraday alignment and detection at two different circular polarization directions. The spectra resemble that of the Voigt configuration (Figure 3b) with minor intensity variations between the circular polarized components. Most importantly, the random orientation of sNRs in the examined specimen leads to reduced polarization ratio by a factor of $(1 \pm \cos \theta)^2$ (θ is the angle between external magnetic field the c-axis of wurtzite structure). The similarity of the circular polarized components to the spectra recorded under a Voigt alignment indicates that the latter is mainly composed of a sum of polarized emission events, but with additional weak contribution from forbidden transitions at low field regions.

Figure 3d displays the ODMR spectrum of an exciton (green) band in CdSe/CdS:Mn sNRs recorded in the Voigt configuration, which was detectable only with low chopping frequencies <90 Hz. The spectrum consists of a dominant positive resonance due to enhancement of luminescence intensity upon MW radiation. It is worth noting that the exciton transition in undoped sNRs did not present any ODMR signal in either the Voigt or the Faraday configuration.

Parts e and f of Figure 3 depict the spectral dependence ODMR (SD-ODMR) curves of undoped (e) and doped (f) sNRs, respectively. Such curves are generated by scanning the PL spectra under the influence of: a magnetic resonance condition, $B_{\rm max}$ of the corresponding ODMR resonances, experimental $v_{\rm MW}$, and chopping frequency of 240 Hz. The corresponding PL curves are drawn for comparison in each figure. Comparing panels (e) and (f) reveals an intensity quench in the red spectral regimes and enhancement in the exciton regime of the doped sNRs, but a lack of magnetic resonance events in the exciton region of the undoped sNRs. The trends shown in Figure 3e,f further supports the appearance of negative and positive resonance signals in Figure 3a–d.

Following the observations in Figure 3, a qualitative model can be presented. Referring to the discussion in the introduction, the sNRs under consideration possess a type-I electronic configuration, and thus the radiative processes occur in the CdSe seed or/and at the seed-rod interface. Exciton (green) emission involves recombination between a heavy-hole (hh) with angular momentum of $J_{hh} = 3/2$ (projections, $m_{hh} = \pm 3/2$) and an electron with a momentum $S_e = 1/2$ (projections, $m_e = \pm 1/2$). The red deep emission band refers to a trap-to-band or/and trap-to-trap recombination. The plausible recombination routes and their manipulation by magnetic resonance transitions are drawn schematically in Figure 4.

The scheme in Figure 4a illustrates a spin manifold based on a heavy hole (m_{hh}) and a free or trapped electron $(m_{(t)e})$ with electron—hole exchange $(J_{(t)e-hh})$. The 4-fold degeneracy of a band-edge exciton is lifted by the application of an external magnetic field, B_0 . Following excitation above the energy band gap, the manifold states become equally populated. The emission takes place from the bright states $\langle \pm 3/2, \mp 1/2 \rangle$ (red wavy arrows) and, after a delay, also from the dark states $\langle \pm 3/2, \pm 1/2 \rangle$ (not shown). Consequently, a depletion of the bright states' population opens a route for magnetic resonance events, converting population from the dark states to the bright ones (yellow arrows). Under these circumstances two possible scenarios exist. In the case of a fast recombination emission

 $(\tau_{\rm rad} \sim {\rm ns})$, particularly with respect to a slow spin-relaxation time $(T_1 \sim {\rm ms})$, thermalization via Boltzmann distribution is excluded. Then magnetic resonance transitions enhance the luminescence intensity. On the contrary, a slow recombination emission allows thermalization among the states on a time scale of <100 ps, ⁵⁹ and consequently, magnetic resonance transitions reverse their direction; thus, a quenching of luminescence intensity occurs. In other words, the observation of either positive (enhancement) or negative (quenching) ODMR signal reflects the competition between the recombination rate and the spin-lattice relaxation rate $(\frac{1}{T_1})$, assuming negligible contributions from other factors such as exciton disposition, or interpretation growing between the deals and

dissociation or intersystem crossing between the dark and bright states. ^{76,80} A probable spectrum is given at the bottom of Figure 4a, showing spin-flip processes of electrons alone (arrows 1 and 2). In the case of a large $J_{(t)e-hh}$ value, those transitions will be resolved; otherwise, their envelope will be detected. Note that a direct flip of a heavy hole projection is forbidden by the need for momentum conservation. Also, it is equally important that a trapped electron (te) at a defect site seizes a spin momentum $S_{te} = 1/2$, and therefore, both bandto-band and trap-to-band recombination follow the same routes as shown in Figure 4a, probably with different radiative rates. The situation is more complex for trapped hole (th) and electron (te) pairs that are involved in trap-to-trap recombination, the spin diagram of which is given in Figure 4b. In most cases, a trapped hole (th) acquires a spin momentum of S_{th} = 1/2, different from that of a valence band edge; thus, a spin-flip transition for both the electron and a hole can take place and each may be split by spin-exchange, J_{te-th} . Accordingly, the radiative transitions in Figure 4b are marked by the red-wavy arrows, and magnetic resonance transitions are shown by the yellow arrows. For simplicity, J_{te-th} is presented here as a scalar variable, but anisotropy in an exchange interaction may exist as well. As will be discussed in the simulations below, a small contribution by such anisotropy is included under a broadening factor. A possible spectrum for $J_{te-th} \neq 0$ is shown at the bottom of the diagram of Figure 4b for an unthermalized situation. But the thermalization among spin states can alter the relative intensities of the resonance transitions or invert their sign from positive to negative. Furthermore, when J_{te-th} is small, the fine details fade (dashed line in the anticipated spectrum). Finally, an ODMR spectrum of an exciton recombination basically appears as a negative signal if a magnetic resonance event happens at a nearby shunting nonradiative state, when the latter depletes the excitonic state's population. Such a case is in contrast with the observation in Figure 3d, and therefore, this scenario is not discussed further.

From the schemes shown in Figure 4, most of the experimental observations can be explained. The ODMR spectrum monitoring the red band emission in undoped sNRs (Figure 3a) is composed of two overlapping features: (1) A trap-to-band recombination that involves a trapped electron and a band-edge heavy hole. In this case, magnetic resonance flips the electron spin alone and leads to a relatively narrow signal (for small J_{te-th}). The negative sign suggests thermalization, in agreement with the long lifetime of the emission (see inset in Figure 2c). (2) A trap-to-trap recombination involving trapped electron and hole, with a long recombination time that allows thermalization. The spin flip of each carrier is only partially resolved, due to small J_{te-th} , as well as due to broadening by a distribution of electron—hole distances

Table 1. Spin Hamiltonian Parameters Used for Simulating the ODMR Observations

sNRs/variable	$g_{xx}^{(t)e} = g_{yy}^{(t)e}$ $g_{zz}^{(t)e}$	$g_{xx}^{hh} = g_{yy}^{hh} g_{zz}^{hh} a$	$g_{xx}^{th} = g_{yy}^{th} g_{zz}^{th} a$	Je-hh (μev)	Je-th (μev)	$J_{(t)e\text{-}Mn} \choose \mu \text{ev}$	$J_{(t)h\text{-}Mn} \ (\mu \text{ev})$	$A_i \ (\mu { m ev})$
CdSe/CdS red emission (Voigt detection)	1.99	-0.81	1.94	0.89	0.93			
	1.92	-0.97	1.74					
CdSe/CdS:Mn red emission (Voigt detection)	1.98	-1.04	1.35	1.0	0.93	-0.03	0.19	0.7
	1.76	-1.02	1.28					
CdSe/CdS:Mn green emission (Voigt detection)	1.99	-0.70		0.89		-0.07	0.327	0.7
	1.82	-0.85						

^ag-factor uncertainty $\pm 0.005 - 0.01$.

(pronounced as a distribution of J_{te-th} values) as well as anisotropy in the value of J_{te-th} . Such broadening is often observed in ODMR spectra of donor-acceptor recombination processes in bulk and nanoscaled semiconductors.⁷⁹ The gfactors of the trapped carriers' resonances in this study are compatible with nearly free spins and differ substantially from those of band-edge carriers in these materials. Notably, the trap-to-band and trap-to-trap processes may share the same localized electron. Previous ODMR studies of core/shell interfaces in colloidal quantum dots suggested the occurrence of a few different stoichiometric defects, including $V_{\mathrm{Cd2+}}$ and $V_{\rm S0}$ vacancies that can accommodate single holes and $V_{\rm Cd0}$ and $V_{\rm S2-}$ vacancies that can accept single electrons. Those defects result from tangential or longitudinal strains⁸¹ that lead to twin boundaries or edge dislocations. 82 Ultimately, the g-factor of a trapped carrier will be different from that of a band-edge carrier, and would depend on the local trapping environment. For example, trapping near heavy metal ions with large spinorbit coupling results in g-factors that deviate from that of a free carrier, whereas trapping next to a chalcogen site leads to g-factors that approach the value of the free carrier (2.002). 83,84 It is worth noting that carrier trapping at external surface site cannot be completely excluded. However, the relatively low temperature growth of the rod (see the SI) tends to induce large concentrations of defects at the seed-rod interface, dominating the trapping process. In addition, the dimensions of the material platform under investigation possess type-I electronic alignment, thus focusing the carriers close to an internal interface. Furthermore, the simulation discussed below exposes g-factor values compatible with electron trapping around heavy metals, while such a carrier at an external or surface position is in large part surrounded by organic ligands. Thus, it is reasonable to assume that the red recombination emission is dominantly related to trapping recombination from interface sites.

The ODMR spectrum of the doped sNRs monitored at the red band (Figure 3b) shows a few components, one of which is related to the trap-to-band recombination as in the undoped derivative. However, the trap-to-trap resonance transition shifted from g=1.903 to 2.002. The spin-Hamiltonian simulation (given below) corroborates the attribution of this shift to a coupling between trapped carriers at interface sites and neighboring $\mathrm{Mn^{2+}}$ spins. Again, the negative sign of the ODMR resonance is associated with thermalization involving a slow recombination time of $\sim\!634$ ns in the red-emission region. The interpretation of the third component in the spectrum of Figure 3b is not as clear, and this feature is probably related to a forbidden magnetic resonance transition with a different spin-relaxation time.

The ODMR spectrum of the green emission of doped sNRs (Figure 3d) can be associated with band-to-band recombina-

tion. However, the electron—hole annihilation is delayed by the interaction with Mn²⁺ spins or self-trapping due to doping, marginally following the experimental time response only at low chopping frequencies. The resonance appears as a positive signal, similar to the nonthermalized case, suitable for an exciton recombination according to the models shown in Figure 4. In contrast to the pronounced green-emission ODMR signal in the doped sNRs, a magnetic resonance effect is missing in the green spectral window of the undoped sNRs. This absence is due to the fast recombination of free excitons in the undoped sNRs, incompatible with the time-response of the ODMR experiment.

The ODMR data in Figure 3 were simulated using the following spin Hamiltonian,³⁴ which includes *various* magnetization parameters based on the diagrams shown in Figure 4.

$$\begin{split} H_{s} &= \mu_{B} \vec{S}_{(t)e} \overline{g}_{(t)e} \vec{B}_{0} + \mu_{B} \vec{J}_{hh} \overline{g}_{hh} \vec{B}_{0} + \mu_{B} \vec{S}_{th} \overline{g}_{th} \vec{B}_{0} \\ &+ \mu_{B} \vec{S}_{Mn} \overline{g}_{Mn} \vec{B}_{0} + J_{(t)e-(t)h} \vec{S}_{(t)e} \vec{S}_{(t)h} + J_{(t)e-Mn} \vec{S}_{(t)e} \vec{S}_{Mn} \\ &+ J_{(t)h-Mn} \vec{S}_{(t)h} \vec{S}_{Mn} + H_{hf} \end{split}$$

$$H_{hf} = \nu_{0} \sum_{i} A_{i}^{I} |\psi(R_{i})|^{2} \vec{S}_{e,h} \langle \vec{I}_{nuclei}^{i} \rangle \tag{1}$$

The first four terms in eq 1 correspond to the Zeeman interactions of (trapped)electron, heavy-hole, trapped-hole, and Mn^{2+} spins, respectively, with spin momentums $S_{(t)e}$, J_{hh} , S_{thv} and S_{Mn} and g-factors $g_{(t)e}$, g_{hhv} , g_{thv} , g_{Mn} , $J_{(t)e-(t)hv}$, $J_{(t)e-Mnv}$, and $J_{(t)h-Mn}$ represent the (trapped)electron—(trapped)hole, (trapped)electron-Mn²⁺, and (trapped)hole-Mn²⁺ interactions. For simplicity, the $S_{(t)h}$ notation is denoted as either J_{hh} or S_{th} in exchange-coupling terms. The values of $J_{(t)e\text{-}Mn}$ and $J_{(t)h-Mn}$ are controlled by the spatial overlap between Mn^{2+} ions and the carrier distribution functions. The coupling constants J_{e-Mn} and J_{hh-Mn} can be evaluated from the expressions $J_{e-Mn} = -\alpha |F_i(R)^2|$ and $J_{hh-Mn} = -\frac{\beta}{3} |F_i(R)^2|$, where $F_i(R)^2$ (i = e, h) refers to a spherical seed and a Mn^{2+} ion is positioned at a distance R from the seed's center. α and β correspond to the electron-Mn and heavy-hole-Mn interaction coefficients, where α refers to s-d coupling and β a p-d interaction, and the latter has a larger value than the former (those values were adopted from the literature).³ While the given expression is suitable for the evaluation of coupling processes with bandedge carriers, they are not suitable for the evaluation of J_{te-Mn} or J_{th-Mn} , so those are left as fitting parameters. The hyperfine term includes various nuclear fields with hyperfine constants A_i , dominated by the Mn²⁺ nuclei but also with some contribution from rare spin-bearing Cd2+ isotopes of the host lattice. In the present case, hyperfine interactions were found to be orders of magnitude weaker than the J-coupling terms, thus having a

negligible effect on the appearance of the ODMR, but they may have an important effect on the spin lifetime. Representative simulations of the ODMR spectra in the undoped and doped sNRs are shown as blue lines in Figure 3a,b,d. The simulated curves in Figure 3a,b are composed of two major magnetic resonance transitions; trap-to-band and trap-to-trap. The simulation of the curve in Figure 3d includes a single band. The simulation variables for *various* transitions are summarized in Table 1.

The variables in Table 1 convey interesting trends: (a) All

Landé *g*-factors are anisotropic, implying localization at asymmetric sites, for example, along the core—shell interface.

(b) The electron Landé ge-factors deviate substantially from that of an electron at the conduction band edge of wurtzite-CdSe (0.68) nanostructures and instead approach the value of a free carrier (2.002). The close proximity of the g_{ε} values to that of a free electron reflects trapping at a site free of spinorbit coupling, e.g., a neutral metal vacancy surrounded by chalcogenide ions, as part of the red-emission of undoped and doped sNRs. (c) The g_{hh} values show some variation but overall are close to those linked with a valence band hole of wurtzite-CdSe (0.98-1.09). Hence, the sharp resonance in the red-emission region in both undoped and doped sNRs is associated with recombination of an interface-trapped electron with a valence band hole. (d) The g-factor values of trapped holes (g_{th}) differ from those of both valence band holes and free carriers. In addition, they also have strong anisotropy, suggesting localization at the core-shell interface, at a site influenced by spin-orbit coupling such as a chalcogenide vacancy (V_{50}) next to surrounding metal cations. Thus, the broad resonances associated with the red emission feature in the undoped and doped sNRs are due to trap-to-trap recombination along the interface, while that of the doped sample is also influenced by carrier-dopant exchange coupling. As a general statement, the resonance g values as read from the experimental data, particularly of the broad resonance transitions, match with the average of the anisotropic factors $\left\{ \sqrt[2]{(g_{xx}^2 + g_{yy}^2 + g_{zz}^2)} \right\}$. (e) The electron-hole exchange coupling $(J_{(t)e-(t)h})$ in most cases is relatively small (~1.0 μeV), reflecting a small overlap between band-to-trap or trapto-trap carrier distribution functions, and as expected it is smaller than the value of ~4 meV reported for a pure excitonic process.⁵⁹ The anisotropy of the exchange term as well as distribution of electron-hole spatial distances, are compensated in the simulation by use of a distribution function of $J_{(t)e-(t)h}$ values. (f) The carrier-dopant coupling constants are in the range of 100 μ eV, mostly showing stronger coupling of the hole with respect to that of the electron (as generally found in II-VI semiconductors). The strong coupling is associated with proximity between interface-trapped carriers and Mn2+ dopants. Simple evaluation of the number of Mn²⁺ ions in close proximity to the interface is given in the SI, revealing ~ 21 dopant ions out of 1718 metal sites. Such a dilution supports the assumption considered in the simulation for the interaction of a single Mn2+ ion with a single trapped carrier at the interface. The simulations of the ODMR spectra of doped sNRs were extremely sensitive to the values of $J_{(t)e-Mn}$ and $J_{(t)h-Mn}$ and their distribution (due to anisotropy or carrier—Mn²⁺ distance), broadening the trap-to-trap magnetic resonance (see test cases at the Figure S7) and washing out the carrier-Mn²⁺ fine structure splitting. The hyperfine coupling is

close to that of Mn²⁺ in the ESR spectrum, with a small influence on the ODMR spectral appearance.

The discussion until this point has focused on identification of the recombining carriers under steady-state conditions. However, temporal information can also be gained by following the dependence of the ODMR spectral shape on the applied MW chopping frequency.³⁴ Figure 5a shows a

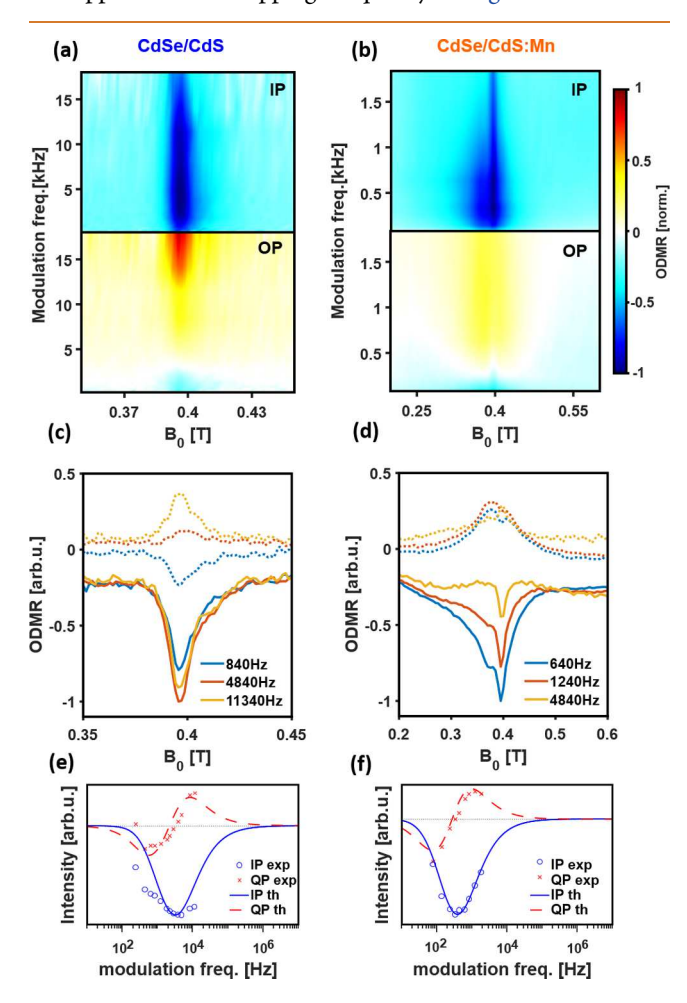


Figure 5. ODMR dependence on the MW chopping frequency: (a, b) contour plots of the ODMR spectra of CdSe/CdS:Mn (a) and CdSe/CdS (b) sNRs, monitored at the red-emission region with Voigt alignment at 2.17 K, under various MW chopping frequencies in-phase (IP) and out-of-phase (OP) with the on-set of MW radiation; (c, d) spectra cuts from the plots in (a, b), respectively, under a few selective MW chopping frequencies in IP (solid) and OP (dashed); (e,f) plot of the ODMR intensity versus the MW chopping frequency for CdSe/CdS:Mn (c) and CdSe/CdS (d) sNRs, based on the data shown in (a, b) and those in Figure S8. A best fit to the chopping frequencies for undoped (left) and doped (right) sNRs bestowing eq 2.

contour map of a set of ODMR spectra monitored at the redemission of the doped sNRs, recorded in the Voigt orientation in-phase (IP) and out-of-phase (OP) with respect to the MW "on" time. Those ODMR data sets reveal evolution of the spectrum's appearance with a change in chopping frequency. Selected raw data are displayed in Figure 5c, while a full set of the raw data is given in Figure S8(a). Following the in-phase evolution, the change in chopping frequency allows deconvolution of *various* components underneath a wide spectral envelope: a sharp band that was assigned to the trap-to-band

recombination maintained a negative sign up to the highest chopping frequency; a broad band that was assigned to the trap-to-trap recombination experienced a drastic intensity reduction with increased chopping rate and eventually turned into a positive signal at the highest chopping frequencies; a third band at low magnetic field (centered at 0.27 T) was revealed at the highest chopping rate and is tentatively assigned as a forbidden transition. Figure 5b shows a contour plot of ODMR spectra of the undoped sNRs recorded in the Voigt alignment, while a few cut spectra at selected chopping frequencies are shown in Figure 5d. The full set of row data associated with the contour plot in Figure 5b is presented in Figure S8(b). The best-fit Gaussians to the in-phase curves illustrate occurrence of two events. The out-of-phase bands in Figure 5a,b are dominated by positive wide bands that are nearly a mirror image of the features recorded in-phase, despite the sharp trap-to-band recombination. Figure S8(c) depicts a few ODMR spectra of the red-emission region in the doped sNRs monitored under Faraday alignment at a few different chopping frequencies. The in-phase curves in Figure S8(b) resemble that of Figure 5b, except for the absence of the lowfield band, supporting its assignment as a forbidden transition that is allowed in the Voigt configuration. Figure S9 displays the chopping frequency dependence of the green-emission ODMR in the doped sNRs.

Figure 5e,f present plots of the integrated intensity over the entire ODMR spectrum *versus* the chopping frequencies of the red-emission in undoped (e) and doped (f) sNRs. It is noteworthy that the output of the lock-in detection mainly preserves the lowest Fourier component of a square-wave, and the latest is related to a transient measure of an ODMR signal by a Fourier transformation. Accordingly, the trends in Figure 5e,f were simulated by a kinetic model according to the following equations⁷⁶

$$\begin{split} \frac{dn_s}{dt} &= G_s - C_s n_s + k_{MW} (n_t - n_s) - k_{ISC} (n_s - F n_s) \\ &+ k_{ISC} (n_t - (1 - F) n_t) \\ \frac{dn_t}{dt} &= G_t - C_t n_t + k_{MW} (n_s - n_t) - k_{ISC} (n_t - (1 - F) n_t) \\ &+ k_{ISC} (n_s - F n_s) \\ F &= (1 + e^{\Delta E/kT})^{-1}; \quad C_{s,t} = r_{s,t} + d_{s,t}; \quad I \propto r_s n_s + r_t n_t \end{split}$$

where $n_{\rm t}$ and $n_{\rm s}$ are the populations of triplet and singlet (dark and bright) spin sublevels, respectively; $G_{\rm t}$ and $G_{\rm s}$ are the generation rates for singlet and triplet pairs; $d_{\rm t}$ and $d_{\rm s}$ are dissociation rates; $r_{\rm t}$ and $r_{\rm s}$ are the recombination rates; $k_{\rm MW}$ describes the rate of the magnetic resonance transitions; $k_{\rm ISC}$ is the intersystem-crossing rate (spin mixing term); F is a Fermi–Dirac thermal distribution function, and ΔE refers to a resonance transition energy. These kinetic equations were solved according to the procedure given in ref 76.

A best fit to the chopping frequencies is shown by the thin lines in Figure 5e,f. The fit parameters are listed in Table 2. A few variables, like $k_{\rm ISC}$, d_s , d_v and r_v were found to be negligible with respect to other dominant factors, corroborating the model shown in Figure 4. The similarity between the trends in panels (e) and (f) suggests a common electron—hole recombination process in undoped and doped sNRs. However, the additional carrier— Mn^{2+} coupling in the doped sNRs is manifested as a shift in the extrema points: The in-phase

Table 2. Kinetic Variables Used for the Simulation of Frequency-Dependence ODMR

parameters	CdSe/CdS	CdSe/CdS:Mn		
$r_{ m S}$	3×10^{4}	2×10^{3}		
$r_{ m t}$	3×10^{3}	3×10^{2}		
$d_{ m s}$	10^{-3}	10^{-5}		
$d_{ m t}$	10^{-4}	10^{-6}		
$K_{ m ISC}$	10^{-4}	10^{-6}		
$K_{ m MW}$	2×10^{3}	10^{3}		
F	0.25	0.25		
$G_{ m S}$	2×10^{14}	2×10^{14}		
G_{t}	2×10^{-13}	2×10^{-12}		

component of doped sNRs exhibits a negative extremum at a frequency higher than that of the undoped sNRs, compatible with a longer lifetime. The r_s values are compatible with long red-emission recombination and also with the thermalized case discussed above.

The spin relaxation time, T_1 , is extracted from out-of-phase component (the period after the turn-off of the MW pulse), shown by the dashed line in Figure 5e,f. The extrema on those curves refer to a condition where the spin decay process reaches a steady state just before the arrival of the following MW pulse, and those points are correlated with $1/T_1$ Hence, the out-of-phase trends exhibited a longer spin-relaxation time in doped sNRs (0.1 μ s) with respect to the undoped sNRs $(0.01 \,\mu\text{s})$. The relatively long T_1 values are commonly found in cases where the examined carriers are free from spin-orbit coupling (SOC), like the trapped carriers in the present case, which are detached from the orbit effect of the valence band. The out-of-phase curves are also characterized by a deflection at a low chopping frequency at zero point, which may be associated with opposing contributions from the various factors or equilibrium saturation within the spin manifold. However, differentiation among these possibilities is unachievable at the current time.

Overall, analysis of the ODMR chopping-frequency dependence allowed deconvolution of overlapping magnetic events and enabled evaluation of the radiative and spin—lattice relaxation rates. The results of this analysis support the proposed model displayed in Figure 4.

CONCLUSIONS

In summary, the present work has focused on the spin properties of undoped and Mn2+-doped sNRs prepared via colloidal procedures, where diluted concentrations of Mn²⁺ ions were installed within the rod volume. The spin properties were examined using ODMR spectroscopy at cryogenic temperatures. The main observations are summarized in a scheme (Figure 6). The low-temperature PL spectra exposed two distinguished spectral regimes, associated with exciton (green) and trap (red) recombination processes. Typical ODMR observations exposed the following recombination routes: band-to-band (green arrow) trap-to-band (left-red arrow), and trap-to-trap (right-red arrow). The related ODMR spectra (given as insets aside to the arrows) revealed an unthermalized process (enhancement of luminescence) for the exciton emission, but a thermalized event (quenching of the luminescence) for the trap-recombination processes. The anisotropy of the magnetic parameters for the trappedrecombination events proposed a localization of carriers around the seed/rod interface (see illustration above the

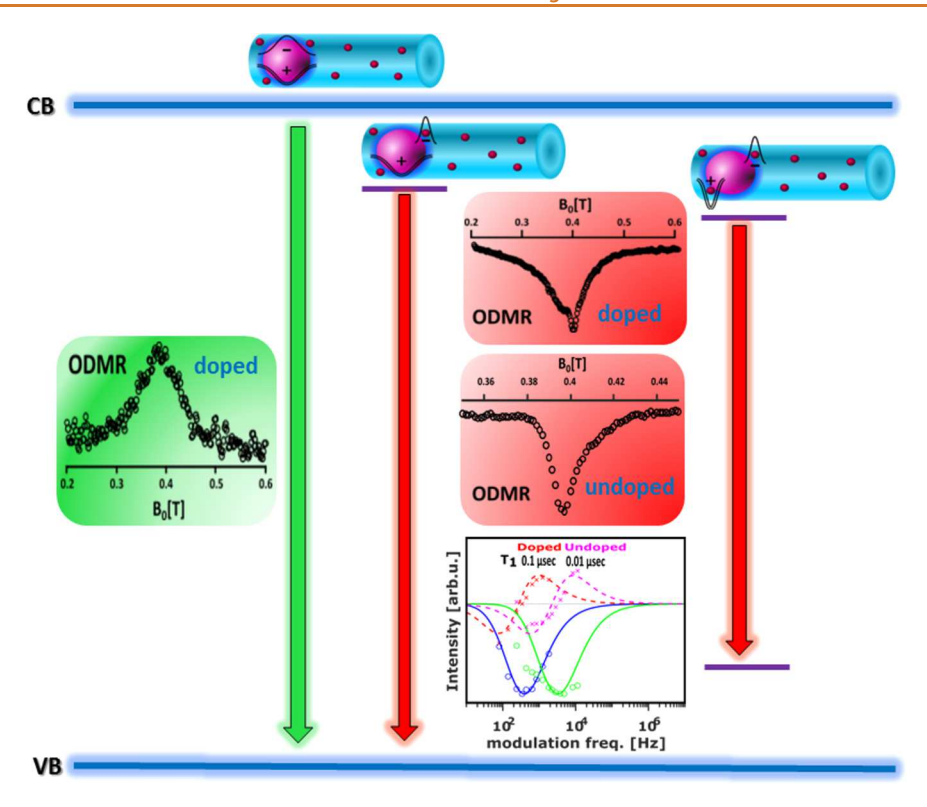


Figure 6. Scheme of recombination processes evolved from the ODMR investigation: The arrows mark the band-to-band (green), trap-to-band (red) and trap-to-trap (red) recombination processes. The relevant carriers' wave functions are displayed schematically above each arrow. The observed ODMR spectrum related to each emission event is displayed aside each arrow. The ODMR chopping modulation dependence of doped and undoped depicts at the bottom of the figure reveals an order of magnitude change in spin-relaxation time (T_1) upon doping.

arrows). A best fit by a kinetic model to the chopping frequency ODMR dependence (bottom inset) revealed information about the ratio of radiative to spin-relaxation rates and showed an extension of the spin relaxation time by coupling with Mn²⁺ dopants. Overall, this work has described interface spin properties in elongated structures and their manipulation by magnetic doping, with importance for the implantation of such structures in spin-based technology.

METHODS

Sample Preparation. CdSe/CdS sNRs were prepared following the synthesis procedure given in ref 47. The method for preparation of CdSe/CdS:Mn sNRs is described in detail in the Supporting Information.

General Characterization. The absorption spectra of the samples were recorded on a JASCO V-570 UV-vis-NIR spectrometer.

The morphology and size of the sNRs and their composition were measured via inspection of the TEM images. The samples were prepared by drop-casting of dilute colloidal suspensions of sNRs in toluene onto ultrathin carbon film, Cu grids 400 mesh, (Ted Pella, Inc.) and measured by transmission electron microscope (TEM): FEI Tecnai G^2 T20 S-Twin TEM with 200 kV acceleration voltage. EDX maps were registered on scanning transmission electron microscope (STEM) with 60 or 200 kV acceleration voltage: FEI Titan Cubed Themis G^2 60-300 equipped with Dual-X detector (Bruker) with an effective solid angle of 1.76 sr.

Electron spin resonance (ESR) was used to confirm incorporation of $\mathrm{Mn^{2+}}$ ions in sNRs at selected position. The ESR spectra were recorded on a Bruker EMX-10/12 X band ($\nu = 9.4~\mathrm{GHz}$) digital ESR spectrometer equipped with a Bruker N2-temperature controller.

Magneto-optical Measurements. Continuous-wave (cw) PL and ODMR measurements. Colloidal sNRs were excited using a 405

nm cw-laser diode, and the spectra were collected using a SpectraPro 300i spectrometer, Si-diode, and Ametek 7270 Lock-in Amplifier. The PL and ODMR measurements were performed inside a Janis 12 CNDT liquid helium cryostat with a Cryomagnetics superconducting magnet that is controlled by an Oxford IPS 120 power supply. Microwave (MW) radiation was generated by a HP 83620A source, which was triggered by a Stanford DG 535 pulse generator. Also, the output of the MW source was amplified by Narda West 60583 MW amplifier, as well as by a custom-made MW cavity. See more details in the SI.

Time-Resolved Measurements. The radiative lifetime $(\tau_{\rm rad})$ was measured by exciting the sample with a PicoQuant LDH-D-C-450 pulsed laser and following the transient PL curves using a Micro Photon Devices (MPD) avalanche photodiode (APD). The spin-relaxation time (T_1) was extracted indirectly from the MW chopping frequency dependence of the ODMR spectrum, as discussed in the text above.

ASSOCIATED CONTENT

Supporting Information

The Supporting Information is available free of charge at https://pubs.acs.org/doi/10.1021/acsnano.0c05454.

Description of the materials' preparation and microscopy characterization of undoped sNRs, description of optical measurements setup, PL time—decay curves, and complementary ODMR spectra in Voigt and Faraday configuration (PDF)

AUTHOR INFORMATION

Corresponding Author

Efrat Lifshitz — Schulich Faculty of Chemistry, Solid State Institute, Russell Berrie Nanotechnology Institute, Technion—Israel Institute of Technology, Haifa 3200003, Israel; oorcid.org/0000-0001-7387-7821; Email: ssefrat@technion.ac.il

Authors

Joanna Dehnel — Schulich Faculty of Chemistry, Solid State
Institute, Russell Berrie Nanotechnology Institute,
Technion—Israel Institute of Technology, Haifa 3200003, Israel
Yahel Barak — Schulich Faculty of Chemistry, Solid State
Institute, Russell Berrie Nanotechnology Institute,
Technion—Israel Institute of Technology, Haifa 3200003, Israel
Itay Meir — Schulich Faculty of Chemistry, Solid State Institute,

Itay Meir — Schulich Faculty of Chemistry, Solid State Institute, Russell Berrie Nanotechnology Institute, Technion—Israel Institute of Technology, Haifa 3200003, Israel

Adam K. Budniak — Schulich Faculty of Chemistry, Solid State Institute, Russell Berrie Nanotechnology Institute, Technion—Israel Institute of Technology, Haifa 3200003, Israel

Anjani P. Nagvenkar — Schulich Faculty of Chemistry, Solid State Institute, Russell Berrie Nanotechnology Institute, Technion—Israel Institute of Technology, Haifa 3200003, Israel

Daniel R. Gamelin — Department of Chemistry and the Molecular Engineering Materials Center, University of Washington, Seattle, Washington 98195-1700, United States; orcid.org/0000-0003-2888-9916

Complete contact information is available at: https://pubs.acs.org/10.1021/acsnano.0c05454

Author Contributions

§J.D. and Y.B. contributed equally.

Notes

The authors declare no competing financial interest.

ACKNOWLEDGMENTS

The authors acknowledge financial support from the European Commission *via* the Marie-Sklodowska Curie action Phonsi (H2020-MSCA-ITN-642656), the Israel Science Foundation (No. 2528/19), the Israel Science Foundation (No. 1045/19), the USA/Israel Binational Science Foundation (No. 2016156), and the joined USA National Science Foundation—USA/Israel Binational Science Foundation (NSF-BSF, No. 2017637). Additional support was provided by the U.S. National Science Foundation (NSF) through project DMR-1807394 and the UW Molecular Engineering Materials Center, a Materials Research Science and Engineering Center (DMR-1719797). The authors express their gratitude to Prof. Alexander Efros for a fruitful discussion and to Dr. Yaron Kauffmann from the Electron Microscopy Center (MIKA) at the Technion for the technical assistance.

REFERENCES

- (1) Ohno, H. Making Nonmagnetic Semiconductors Ferromagnetic. *Science* **1998**, 281, 951–956.
- (2) Gislason, H. P.; Monemar, B.; Dean, P. J.; Herbert, D. C.; Depinna, S.; Cavenett, B. C.; Killoran, N. Photoluminescence Studies of the 1.911-EV Cu-Related Complex in GaP. *Phys. Rev. B: Condens. Matter Mater. Phys.* **1982**, 26, 827–845.
- (3) Furdyna, J. K. Diluted Magnetic Semiconductors. J. Appl. Phys. 1988, 64, R29–R64.
- (4) Jun, Y.; Jung, Y.; Cheon, J. Architectural Control of Magnetic Semiconductor Nanocrystals. J. Am. Chem. Soc. 2002, 124, 615–619.
- (5) Besombes, L.; Leger, Y.; Maingault, L.; Ferrand, D.; Mariette, H.; Cibert, J. Probing the Spin State of a Single Magnetic Ion in an Individual Quantum Dot. *Phys. Rev. Lett.* **2004**, *93*, 207403.

- (6) Besombes, L.; Leger, Y.; Maingault, L.; Ferrand, D.; Mariette, H.; Cibert, J. Carrier-Induced Spin Splitting of an Individual Magnetic Atom Embedded in a Quantum Dot. *Phys. Rev. B: Condens. Matter Mater. Phys.* **2005**, *71*, 161307.
- (7) Furdyna, J. K.; Kossut, J. Diluted Magnetic Semiconductors; Willardson, R. K., Beer, A. C., Eds.; Academic Press: London, 1988; Semiconductors and Semimetals, Vol. 25.
- (8) Yoder-Short, D. R.; Debska, U.; Furdyna, J. K. Lattice Parameters of $Zn_{1-x}Mn_xSe$ and Tetrahedral Bond Lengths in $A^{II}_{1-x}Mn_xB^{VI}$ Alloys. *J. Appl. Phys.* **1985**, *58*, 4056–4060.
- (9) Beaulac, R.; Schneider, L.; Archer, P. I.; Bacher, G.; Gamelin, D. R. Light-Induced Spontaneous Magnetization in Doped Colloidal Ouantum Dots. *Science* **2009**, *325*, 973–976.
- (10) Beaulac, R.; Archer, P. I.; Ochsenbein, S. T.; Gamelin, D. R. Mn²⁺-Doped CdSe Quantum Dots: New Inorganic Materials for Spin-Electronics and Spin-Photonics. *Adv. Funct. Mater.* **2008**, *18*, 3873–3891.
- (11) Beaulac, R.; Archer, P. I.; Liu, X.; Lee, S.; Salley, G. M.; Dobrowolska, M.; Furdyna, J. K.; Gamelin, D. R. Spin-Polarizable Excitonic Luminescence in Colloidal Mn²⁺-Doped CdSe Quantum Dots. *Nano Lett.* **2008**, *8*, 1197–1201.
- (12) Norris, D. J.; Efros, A. L.; Erwin, S. C. Doped Nanocrystals. *Science* **2008**, *319*, 1776–1779.
- (13) Rami, B.; Stefan, O.; Daniel, G.; Beaulac, R.; Ochsenbein, S. T.; Gamelin, D. R. Colloidal Transition-Metal-Doped Quantum Dots. In *Nanocrystal Quantum Dots*, 2nd ed.; Klimov, V. I., Ed.; CRC Press: Boca Raton, 2010; pp 397–453.
- (14) Suyver, J. F.; Wuister, S. F.; Kelly, J. J.; Meijerink, A. Luminescence of Nanocrystalline ZnSe: Mn²⁺. *Phys. Chem. Chem. Phys.* **2000**, *2*, 5445–5448.
- (15) Fainblat, R.; Frohleiks, J.; Muckel, F.; Yu, J. H.; Yang, J.; Hyeon, T.; Bacher, G. Quantum Confinement-Controlled Exchange Coupling in Manganese(II)-Doped CdSe Two-Dimensional Quantum Well Nanoribbons. *Nano Lett.* **2012**, *12*, 5311–5317.
- (16) Yu, J. H.; Liu, X.; Kweon, K. E.; Joo, J.; Park, J.; Ko, K.-T.; Lee, D. W.; Shen, S.; Tivakornsasithorn, K.; Son, J. S.; Park, J.-H.; Kim, Y.-W.; Hwang, G. S.; Dobrowolska, M.; Furdyna, J. K.; Hyeon, T. Giant Zeeman Splitting in Nucleation-Controlled Doped CdSe:Mn²⁺ Quantum Nanoribbons. *Nat. Mater.* **2010**, *9*, 47–53.
- (17) Delikanli, S.; Akgul, M. Z.; Murphy, J. R.; Barman, B.; Tsai, Y.; Scrace, T.; Zhang, P.; Bozok, B.; Hernández-Martínez, P. L.; Christodoulides, J.; Cartwright, A. N.; Petrou, A.; Demir, H. V. Mn²⁺ -Doped CdSe/CdS Core/Multishell Colloidal Quantum Wells Enabling Tunable Carrier—Dopant Exchange Interactions. *ACS Nano* **2015**, *9*, 12473—12479.
- (18) Murphy, J. R.; Delikanli, S.; Scrace, T.; Zhang, P.; Norden, T.; Thomay, T.; Cartwright, A. N.; Demir, H. V.; Petrou, A. Time-Resolved Photoluminescence Study of CdSe/CdMnS/CdS Core/Multi-Shell Nanoplatelets. *Appl. Phys. Lett.* **2016**, *108*, 242406.
- (19) Merkulov, I. A.; Yakovlev, D. R.; Keller, A.; Ossau, W.; Geurts, J.; Waag, A.; Landwehr, G.; Karczewski, G.; Wojtowicz, T.; Kossut, J. Kinetic Exchange between the Conduction Band Electrons and Magnetic Ions in Quantum-Confined Structures. *Phys. Rev. Lett.* **1999**, 83, 1431–1434.
- (20) Beaulac, R.; Feng, Y.; May, J. W.; Badaeva, E.; Gamelin, D. R.; Li, X. Orbital Pathways for Mn²⁺-Carrier Sp-d Exchange in Diluted Magnetic Semiconductor Quantum Dots. *Phys. Rev. B: Condens. Matter Mater. Phys.* **2011**, 84, 195324.
- (21) Glazov, M. M.; Ivchenko, E. L.; Besombes, L.; Léger, Y.; Maingault, L.; Mariette, H. Fine Structure of Exciton Excited Levels in a Quantum Dot with a Magnetic Ion. *Phys. Rev. B: Condens. Matter Mater. Phys.* **2007**, 75, 205313.
- (22) Fainblat, R.; Barrows, C. J.; Hopmann, E.; Siebeneicher, S.; Vlaskin, V. A.; Gamelin, D. R.; Bacher, G. Giant Excitonic Exchange Splittings at Zero Field in Single Colloidal CdSe Quantum Dots Doped with Individual Mn²⁺ Impurities. *Nano Lett.* **2016**, *16*, 6371–6377
- (23) Bacher, G.; Maksimov, A. A.; Schömig, H.; Kulakovskii, V. D.; Welsch, M. K.; Forchel, A.; Dorozhkin, P. S.; Chernenko, A. V.; Lee,

- S.; Dobrowolska, M.; Furdyna, J. K. Monitoring Statistical Magnetic Fluctuations on the Nanometer Scale. *Phys. Rev. Lett.* **2002**, *89*, 127201.
- (24) Nelson, H. D.; Bradshaw, L. R.; Barrows, C. J.; Vlaskin, V. A.; Gamelin, D. R. Picosecond Dynamics of Excitonic Magnetic Polarons in Colloidal Diffusion-Doped $Cd_{1-x}Mn_x$ Se Quantum Dots. *ACS Nano* **2015**, *9*, 11177.
- (25) Rice, W. D.; Liu, W.; Baker, T. A.; Sinitsyn, N. A.; Klimov, V. I.; Crooker, S. A. Revealing Giant Internal Magnetic Fields Due to Spin Fluctuations in Magnetically Doped Colloidal Nanocrystals. *Nat. Nanotechnol.* **2016**, *11*, 137–142.
- (26) Yakovlev, D. R.; Ossau, W. Magnetic Polarons. In *Introduction to the Physics of Diluted Magnetic Semiconductors*; Kossut, J., Gaj, J. A., Eds.; Springer-Verlag: Heidelberg, 2010; Chapter 7, pp 221–262.
- (27) Yakovlev, D. R.; Merkulov, I. A. Spin and Energy Transfer between Carriers, Magnetic Ions, and Lattice. In *Introduction to the Physics of Diluted Magnetic Semiconductors*; Kossut, J., Gaj, J. A., Eds.; Springer-Verlag: Heidelberg, 2010; Chapter 8, pp 263–304.
- (28) Awschalom, D. D.; Hong, J. M.; Chang, L. L.; Grinstein, G. Dimensional-Crossover Studies of Magnetic Susceptibility in Diluted-Magnetic-Semiconductor Superlattices. *Phys. Rev. Lett.* **1987**, 59, 1733.
- (29) Govorov, A. O.; Kalameitsev, A. V. Optical Properties of a Semiconductor Quantum Dot with a Single Magnetic Impurity: Photoinduced Spin Orientation. *Phys. Rev. B: Condens. Matter Mater. Phys.* **2005**, *71*, 35338.
- (30) Besombes, L.; Leger, Y.; Bernos, J.; Boukari, H.; Mariette, H.; Poizat, J. P.; Clement, T.; Fernaandez-Rossier, J.; Aguado, R. Optical Probing of Spin Fluctuations of a Single Paramagnetic Mn Atom in a Semiconductor Quantum Dot. *Phys. Rev. B: Condens. Matter Mater. Phys.* **2008**, 78, 125324.
- (31) Oh, E.; Ramdas, A. K.; Furdyna, J. K. Magneto-Optic Phenomena in II-VI Diluted Magnetic Semiconductors: The Faraday and the Voigt Effect. *J. Lumin.* **1992**, *52*, 183–191.
- (32) Fernández-Rossier, J. Single-Exciton Spectroscopy of Semi-magnetic Quantum Dots. *Phys. Rev. B: Condens. Matter Mater. Phys.* **2006**, 73, 045301.
- (33) Grumbach, N.; Rubin-Brusilovski, A.; Maikov, G. I.; Tilchin, E.; Lifshitz, E. Manipulation of Carrier—Mn²⁺ Exchange Interaction in CdTe/CdSe Colloidal Quantum Dots by Controlled Positioning of Mn²⁺ Impurities. *J. Phys. Chem. C* **2013**, *117*, 21021–21027.
- (34) Strassberg, R.; Delikanli, S.; Barak, Y.; Dehnel, J.; Kostadinov, A.; Maikov, G.; Hernandez-Martinez, P. L.; Sharma, M.; Demir, H. V.; Lifshitz, E. Persuasive Evidence for Electron-Nuclear Coupling in Diluted Magnetic Colloidal Nanoplatelets Using Optically Detected Magnetic Resonance Spectroscopy. *J. Phys. Chem. Lett.* **2019**, *10*, 4437–4447.
- (35) Bussian, D. A.; Crooker, S. A.; Yin, M.; Brynda, M.; Efros, A. L.; Klimov, V. I. Tunable Magnetic Exchange Interactions in Manganese-Doped Inverted Core-Shell ZnSe-CdSe Nanocrystals. *Nat. Mater.* **2009**, *8*, 35–40.
- (36) Yang, L.; Knowles, K. E.; Gopalan, A.; Hughes, K. E.; James, M. C.; Gamelin, D. R. One-Pot Synthesis of Monodisperse Colloidal Copper-Doped CdSe Nanocrystals Mediated by Ligand-Copper Interactions. *Chem. Mater.* **2016**, *28*, 7375–7384.
- (37) Shornikova, E. V.; Yakovlev, D. R.; Tolmachev, D. O.; Yu Ivanov, V.; Kalitukha, I. V.; Sapega, V. F.; Kudlacik, D.; Kusrayev, Y. G.; Golovatenko, A. A.; Shendre, S.; Delikanli, S.; Volkan Demir, H.; Bayer, M. Magneto-Optics of Excitons Interacting with Magnetic Ions in CdSe/CdMnS Colloidal Nanoplatelets. *ACS Nano* 2020, *14*, 9032.
- (38) DiVincenzo, D. P. Quantum Computation. Science 1995, 270, 255-261.
- (39) Loss, D.; DiVincenzo, D. P. Quantum Computation with Quantum Dots. *Phys. Rev. A: At., Mol., Opt. Phys.* **1998**, *57*, 120.
- (40) Wolf, S. A.; Awschalom, D. D.; Buhrman, R. A.; Daughton, J. M.; von Molnar, S.; Roukes, M. L.; Chtchelkanova, A. Y.; Treger, D. M. Spintronics: A Spin-Based Electronics Vision for the Future. *Science* **2001**, 294, 1488–1495.

- (41) Hirohata, A.; Takanashi, K. Future Perspectives for Spintronic Devices. *J. Phys. D: Appl. Phys.* **2014**, *47*, 193001.
- (42) Muckel, F.; Barrows, C. J.; Graf, A.; Schmitz, A.; Erickson, C. S.; Gamelin, D. R.; Bacher, G. Current-Induced Magnetic Polarons in a Colloidal Quantum-Dot Device. *Nano Lett.* **2017**, *17*, 4768–4773.
- (43) Zavelani-Rossi, M.; Lupo, M. G.; Tassone, F.; Manna, L.; Lanzani, G. Suppression of Biexciton Auger Recombination in CdSe/CdS Dot/Rods: Role of the Electronic Structure in the Carrier Dynamics. *Nano Lett.* **2010**, *10*, 3142–3150.
- (44) Rabouw, F. T.; Lunnemann, P.; van Dijk-Moes, R. J. A.; Frimmer, M.; Pietra, F.; Koenderink, A. F.; Vanmaekelbergh, D. D. Reduced Auger Recombination in Single CdSe/CdS Nanorods by One-Dimensional Electron Delocalization. *Nano Lett.* **2013**, *13*, 4884–4892.
- (45) Klimov, V. I.; Mikhailovsky, A. A.; Xu, S.; Malko, A.; Hollingsworth, J. A.; Leatherdale, C. A.; Eisler, H. J.; Bawendi, M. G. Optical Gain and Stimulated Emission in Nanocrystal Quantum Dots. *Science* **2000**, *290*, 314–317.
- (46) Rabouw, F. T.; Lunnemann, P.; van Dijk-Moes, R. J. A.; Frimmer, M.; Pietra, F.; Koenderink, A. F.; Vanmaekelbergh, D. D. Reduced Auger Recombination in Single CdSe/CdS Nanorods by One-Dimensional Electron Delocalization. *Nano Lett.* **2013**, *13*, 4884—4892
- (47) Carbone, L.; Nobile, C.; De Giorgi, M.; Sala, F. D.; Morello, G.; Pompa, P.; Hytch, M.; Snoeck, E.; Fiore, A.; Franchini, I. R.; Nadasan, M.; Silvestre, A. F.; Chiodo, L.; Kudera, S.; Cingolani, R.; Krahne, R.; Manna, L. Synthesis and Micrometer-Scale Assembly of Colloidal CdSe/CdS Nanorods Prepared by a Seeded Growth Approach. *Nano Lett.* 2007, 7, 2942–2950.
- (48) Sitt, A.; Sala, F. D.; Menagen, G.; Banin, U. Multiexciton Engineering in Seeded Core/Shell Nanorods: Transfer from Type-I to Quasi-Type-II Regimes. *Nano Lett.* **2009**, *9*, 3470–3476.
- (49) Steiner, D.; Dorfs, D.; Banin, U.; Della Sala, F.; Manna, L.; Millo, O. Determination of Band Offsets in Heterostructured Colloidal Nanorods Using Scanning Tunneling Spectroscopy. *Nano Lett.* **2008**, *8*, 2954–2958.
- (50) Morello, G.; Della Sala, F.; Carbone, L.; Manna, L.; Maruccio, G.; Cingolani, R.; De Giorgi, M. Intrinsic Optical Nonlinearity in Colloidal Seeded Grown CdSe/CdS Nanostructures: Photoinduced Screening of the Internal Electric Field. *Phys. Rev. B: Condens. Matter Mater. Phys.* **2008**, *78*, 1–8.
- (51) Muller, J.; Lupton, J. M.; Lagoudakis, P. G.; Schindler, F.; Koeppe, R.; Rogach, A. L.; Feldmann, J.; Talapin, D. V.; Weller, H. Wave Function Engineering in Elongated Semiconductor Nanocrystals with Heterogeneous Carrier Confinement. *Nano Lett.* **2005**, *S*, 2044–2049.
- (52) Luo, Y.; Wang, L.-W. Electronic Structures of the CdSe/CdS Core-Shell Nanorods. ACS Nano 2010, 4, 91–98.
- (53) Lupo, M. G.; Della Sala, F.; Carbone, L.; Zavelani-Rossi, M.; Fiore, A.; Lüer, L.; Polli, D.; Cingolani, R.; Manna, L.; Lanzani, G. Ultrafast Electron—Hole Dynamics in Core/Shell CdSe/CdS Dot/Rod Nanocrystals. *Nano Lett.* **2008**, *8*, 4582—4587.
- (54) Bronstein, N. D.; Li, L.; Xu, L.; Yao, Y.; Ferry, V. E.; Alivisatos, A. P.; Nuzzo, R. G. Luminescent Solar Concentration with Semiconductor Nanorods and Transfer-Printed Micro-Silicon Solar Cells. *ACS Nano* **2014**, *8*, 44–53.
- (55) Aronovitch, E.; Kalisman, P.; Houben, L.; Amirav, L.; Bar-Sadan, M. Stability of Seeded Rod Photocatalysts: Atomic Scale View. *Chem. Mater.* **2016**, 28, 1546–1552.
- (56) Amirav, L.; Alivisatos, A. P. Photocatalytic Hydrogen Production with Tunable Nanorod Heterostructures. *J. Phys. Chem. Lett.* **2010**, *1*, 1051–1054.
- (57) Hadar, I.; Philbin, J. P.; Panfil, Y. E.; Neyshtadt, S.; Lieberman, I.; Eshet, H.; Lazar, S.; Rabani, E.; Banin, U. Semiconductor Seeded Nanorods with Graded Composition Exhibiting High Quantum-Yield, High Polarization, and Minimal Blinking. *Nano Lett.* **2017**, *17*, 2524–2531.

- (58) Sitt, A.; Hadar, I.; Banin, U. Band-Gap Engineering, Optoelectronic Properties and Applications of Colloidal Heterostructured Semiconductor Nanorods. *Nano Today* **2013**, *8*, 494–513.
- (59) Siebers, B.; Biadala, L.; Yakovlev, D. R.; Rodina, A. V.; Aubert, T.; Hens, Z.; Bayer, M. Exciton Spin Dynamics and Photoluminescence Polarization of CdSe/CdS Dot-in-Rod Nanocrystals in High Magnetic Fields. *Phys. Rev. B: Condens. Matter Mater. Phys.* **2015**, *91*, 155304.
- (60) Granados Del Águila, A.; Jha, B.; Pietra, F.; Groeneveld, E.; De Mello Donegá, C.; Maan, J. C.; Vanmaekelbergh, D.; Christianen, P. C. M. Observation of the Full Exciton and Phonon Fine Structure in CdSe/CdS Dot-in-Rod Heteronanocrystals. *ACS Nano* **2014**, *8*, 5921–5931
- (61) van Schooten, K. J.; Huang, J.; Baker, W. J.; Talapin, D. V.; Boehme, C.; Lupton, J. M. Spin-Dependent Exciton Quenching and Spin Coherence in CdSe/CdS Nanocrystals. *Nano Lett.* **2013**, *13*, 65–71
- (62) Van Schooten, K. J.; Huang, J.; Talapin, D. V.; Boehme, C.; Lupton, J. M. Spin-Dependent Electronic Processes and Long-Lived Spin Coherence of Deep-Level Trap Sites in CdS Nanocrystals. *Phys. Rev. B: Condens. Matter Mater. Phys.* **2013**, *87*, 1–8.
- (63) Vlaskin, V. A.; Barrows, C. J.; Erickson, C. S.; Gamelin, D. R. Nanocrystal Diffusion Doping. *J. Am. Chem. Soc.* **2013**, *135*, 14380–14389.
- (64) Zheng, W.; Wang, Z.; Wright, J.; Goundie, B.; Dalal, N. S.; Meulenberg, R. W.; Strouse, G. F. Probing the Local Site Environments in Mn:CdSe Quantum Dots. J. Phys. Chem. C 2011, 115, 23305–23314.
- (65) Nag, A.; Sapra, S.; Nagamani, C.; Sharma, A.; Pradhan, N.; Bhat, S. V.; Sarma, D. D. A Study of Mn²⁺ Doping in CdS Nanocrystals. *Chem. Mater.* **2007**, *19*, 3252–3259.
- (66) Dorain, P. B. Electron Paramagnetic Resonance of Manganese (II) in Hexagonal Zinc Oxide and Cadmium Sulfide Single Crystals. *Phys. Rev.* **1958**, *112*, 1058–1060.
- (67) Barrows, C. J.; Fainblat, R.; Gamelin, D. R. Excitonic Zeeman Splittings in Colloidal CdSe Quantum Dots Doped with Single Magnetic Impurities. *J. Mater. Chem. C* **2017**, *5*, 5232–5238.
- (68) Magana, D.; Perera, S. C.; Harter, A. G.; Dalal, N. S.; Strouse, G. F. Switching-On Superparamagnetism in Mn/CdSe Quantum Dots. J. Am. Chem. Soc. 2006, 128, 2931–2939.
- (69) Beaulac, R.; Archer, P. I.; Van Rijssel, J.; Meijerink, A.; Gamelin, D. R. Exciton Storage by Mn²⁺ in Colloidal Mn²⁺-Doped CdSe Quantum Dots. *Nano Lett.* **2008**, *8*, 2949–2953.
- (70) Beaulac, R.; Gamelin, D. R. Two-Center Formulation of Mn²⁺-Electron *s-d* Exchange Coupling in Bulk and Quantum-Confined Diluted Magnetic Semiconductors. *Phys. Rev. B: Condens. Matter Mater. Phys.* **2010**, 82, 224401.
- (71) Cavenett, B. C. Optically Detected Magnetic Resonance (O.D.M.R.) Investigations of Recombination Processes in Semi-conductors. *Adv. Phys.* **1981**, *30*, 475–538.
- (72) Shinar, J.; Swanson, L. S. Optically Detected Magnetic Resonance (ODMR) Studies of Conducting Polymers: An Overview. *Synth. Met.* **1992**, *50*, 621–630.
- (73) Lifshitz, E.; Fradkin, L.; Glozman, A.; Langof, L. Optically Detected Magnetic Resonance Studies of Colloidal Semiconductor Nanocrystals. *Annu. Rev. Phys. Chem.* **2004**, *55*, 509–557.
- (74) Litvin, I. D.; Porteanu, H.; Lifshitz, E.; Lipovskii, A. A. Optically Detected Magnetic Resonance Studies of CdS Nanoparticles Grown in Phosphate Glass. *J. Cryst. Growth* **1999**, *198–199*, 313–315.
- (75) Lifshitz, E.; Bykov, L.; Yassen, M. An Optically Detected Magnetic Resonance Study of Laser Ablation Grown PbI2 Epitaxial Films. *J. Phys. Chem.* **1995**, *99*, 15262–15268.
- (76) Lee, S. Y.; Paik, S.; McCamey, D. R.; Boehme, C. Modulation Frequency Dependence of Continuous-Wave Optically/Electrically Detected Magnetic Resonance. *Phys. Rev. B: Condens. Matter Mater. Phys.* **2012**, *86*, 13–16.
- (77) Glozman, A.; Lifshitz, E.; Hoppe, K.; Rogach, A. L.; Welllr, H.; Echymüller, A. Optically Detected Magnetic Resonance of Thiol-Capped CdTe Nanocrystals. *Isr. J. Chem.* **2001**, *41*, 39.

- (78) Langof, L.; Fradkin, L.; Ehrenfreund, E.; Lifshitz, E.; Micic, O. I.; Nozik, A. J. Colloidal InP/ZnS Core-Shell Nanocrystals Studied by Linearly and Circularly Polarized Photoluminescence. *Chem. Phys.* **2004**, 297, 93–98.
- (79) Lifshitz, E.; Glozman, A.; Litvin, I. D.; Porteanu, H. Optically Detected Magnetic Resonance Studies of the Surface/Interface Properties of II VI. J. Phys. Chem. B 2000, 104, 10449–10461.
- (80) Langof, L.; Ehrenfreund, E.; Lifshitz, E.; Micic, O. I.; Nozik, A. J. Continuous-Wave and Time-Resolved Optically Detected Magnetic Resonance Studies of Nonetched/Etched InP Nanocrystals. *J. Phys. Chem. B* **2002**, *106*, 1606–1612.
- (81) Rubin-Brusilovski, A.; Jang, Y.; Shapiro, A.; Safran, A.; Sashchiuk, A.; Lifshitz, E. Influence of Interfacial Strain on Optical Properties of PbSe/PbS Colloidal Quantum Dots. *Chem. Mater.* **2016**, 28, 9056–9063.
- (82) Lifshitz, E.; Porteanu, H.; Glozman, A.; Weller, H.; Pflughoefft, M.; Echymuller, A. Optically Detected Magnetic Resonance Study of CdS/HgS/CdS Quantum Dot Quantum Wells. *J. Phys. Chem. B* **1999**, 103, 6870–6875.
- (83) Lifshitz, E.; Fradkin, L.; Glozman, A.; Langof, L. Optically Detected Magnetic Resonance Studies of Colloidal Semiconductor Nanocrystals. *Annu. Rev. Phys. Chem.* **2004**, *55*, 509–557.
- (84) Emanuelsson, P.; Omling, P.; Meyer, B. K.; Wienecke, M.; Schenk, M. Identification of the Cadmium Vacancy in CdTe by Electron Paramagnetic Resonance. *Phys. Rev. B: Condens. Matter Mater. Phys.* 1993, 47, 15578–15580.